ACS APPLIED NANO MATERIALS

www.acsanm.org

Article

Noninvasive Sensors for Brain−Machine Interfaces Based on Micropatterned Epitaxial Graphene

Shaikh Nayeem Faisal, Tien-Thong Nguyen Do, Tasauf Torzo, Daniel Leong, Aiswarya Pradeepkumar, Chin-Teng Lin, and Francesca Iacopi*

Cite This: *ACS Appl. Nano Mater.* 2023, 6, 5440−5447

Read Online

ACCESS | Metrics & More | Article Recommendations | Supporting Information

ABSTRACT: The availability of accurate and reliable dry sensors for electroencephalography (EEG) is vital to enable large-scale deployment of brain−machine interfaces (BMIs). However, dry sensors invariably show poorer performance compared to the gold standard Ag/AgCl wet sensors. The loss of performance with dry sensors is even more evident when monitoring the signal from hairy and curved areas of the scalp, requiring the use of bulky and uncomfortable acicular sensors. This work demonstrates three-dimensional micropatterned sensors based on a subnanometer-thick epitaxial graphene for detecting the EEG signal from the challenging occipital region of the scalp. The occipital region, corresponding to the visual cortex of the brain, is key to the implementation of BMIs based on the common steady-state visually evoked potential paradigm. The patterned epitaxial graphene sensors show efficient on-skin contact with low impedance and can achieve comparable signal-to-noise ratios against wet sensors. Using these sensors, we have also demonstrated hands-free communication with a quadruped robot through brain activity.

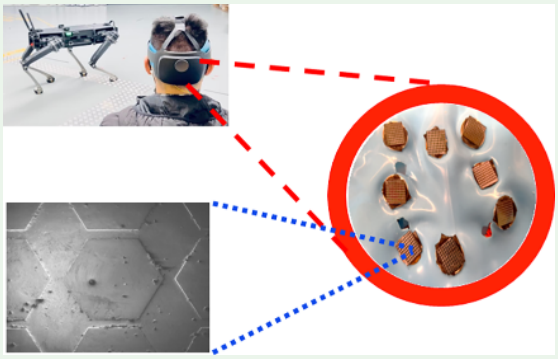

KEYWORDS: *brain−machine interfaces, brain−robot interfaces, epitaxial graphene, photolithography, micropatterned sensors, electroencephalography*

1. INTRODUCTION

Brain−machine interfaces (BMIs) are hands-free and voice-command-free communication systems that allow an individual to operate external devices through brain waves, with vast potential for future robotics, bionic prosthetics, neurogaming, electronics, and autonomous vehicles.[1−4] Such systems typically consist of three modules: an external sensory stimulus, a sensing interface, and a neural signal processing unit.[1,5] Among these, the sensing interface plays a crucial part by detecting the cortical electrical activity, which encodes human intent (brain waves at a frequency of ∼1−150 Hz), through either implanted[6,7] or wearable[8,9] neural sensors, such as electroencephalography (EEG) electrodes.[6−10] Noninvasive sensors are often preferred when no severe disabilities are involved.[9−11] Ag/AgCl-based wet sensors are the reference in terms of performance among the noninvasive electrodes thanks to their low on-skin (∼5−30 kΩ at 50 Hz) impedance and high signal-to-noise (S/N) ratio (30 ± 5 dB).[12,13] However, their use relies on applying a conductive gel electrolyte on the scalp and hair.[13] The use of the gel contributes to skin irritation, risk of infection, hair fouling, allergic reaction, instability upon motion of the individual, and unsuitability for long-term operation due to the gradual drying of the gel.[5,14] Dry sensors have been developed to counter those limitations and enable a portable EEG outside a lab or a clinic.[15−17] The contact impedance (>200 kΩ at 50 Hz) and S/N ratio (5 ± 3 dB) of conventional dry sensors still compare unfavorably to those of the wet sensors.[12,18] In addition, the electrical contact on hairy scalp areas is even more challenging for dry sensors.

Nanometer-thick two-dimensional nanomaterials, especially graphene and graphene derivatives, are promising electrode materials for dry BMI sensors.[19,20] Their very thin nature, combined with high electrical conductivity, biocompatibility, corrosion resistance, and stability in sweat, are all very attractive characteristics for use as sensors for both invasive and noninvasive neural interfaces.[21−25] However, most of the reported noninvasive sensors based on two-dimensional materials typically consist of thin-film electrodes with a flat surface (such as tattoo sensors, e-skin, and e-textrodes) and are not compatible with application on hairy areas of the scalp.[20,26−30] In order to measure the EEG signals from the occipital region of the head,[15] which corresponds to the visual cortex and is thus key for BMIs that rely on visual stimuli, the

Received: December 29, 2022
Accepted: February 24, 2023
Published: March 16, 2023

sensors need to be placed on the back of the head, typically covered by hair. As a reference, a typical human hair diameter is around 80 ± 10 μm, and the density is around 160 ± 10 hairs/cm^2.[31] A recent report on MXene-based EEG sensors showed the advantage of having a three-dimensional pattern by infusing a MXene dispersion in a three-dimensional cellulose structure to detect EEG signals through the hair (5 mm in length).[30]

Moreover, the occipital area of the head possesses a strongly curved surface. Hence, obtaining adequate contact using flat-surface electrodes on the hairy and uneven occipital scalp area is particularly challenging.

In our previous work, we successfully detected high-quality EEG signals from the frontal region of the head using noninvasive epitaxial graphene (EG) sensors on silicon carbide (SiC) on silicon with an unpatterned surface.[32] Here, with the scope of showing the value of this approach for BMIs, we aim at sensing in correspondence to the occipital lobe and demonstrate the use of a steady-state visually evoked potential (SSVEP)[33] paradigm to command an external quadruped robot. The SSVEP paradigm is based on the stimulation through visual inputs flashing at specific frequencies. The individual focuses on the chosen visual command/frequency, inducing identifiable correlated features in the brain activity detected from the occipital cortex.[5,33] To solve the challenge of detecting the EEG signal from the hairy and highly curved occipital scalp, we have fabricated and demonstrated three-dimensional micropatterned EG sensors in a complete BMI system.

2. EXPERIMENTAL PROCEDURE

2.1. EG Synthesis. Cubic silicon carbide (3C-SiC) films epitaxially grown on highly doped Si(100) substrates were purchased from NOVASiC; a chemical and mechanical polishing procedure was performed [StepSiC by NOVASiC (France)].[34] The SiC layer thickness was ∼500 nm. A catalytic alloy approach was employed for the growth of EG on SiC on silicon.[35,36] The physical vapor deposition (PVD) technique was used for the sequential deposition of a Ni layer (∼10 nm) followed by a Cu layer (∼20 nm) using NanoPVD S10A equipment. Annealing the metal-coated samples at ∼1100 °C for 1 h under vacuum conditions (∼10^{-5} bar) leads to breaking of the Si−C bonds thanks to the presence of Ni and the release of the C atoms, which form graphene on the surface. Nickel silicides are the byproducts of this process, which are later removed together with any metal residues on the surface using chemical wet etching for 9 h (Freckle solution).[32] EG/SiC/Si coupons of 1 × 1 cm^2 were used for this study.

2.2. Micropatterned EG Synthesis. The 3C-SiC films epitaxially grown on highly doped silicon substrates were used as a starting material. After photolithography, the 3C-SiC coupons were etched by reactive ion etching (RIE; ICP RIE Oxford Plasmalab 100) by flowing 40 cm^3 STP/min SF_6 and 2 cm^3 STP/min O_2 for 3 min 10 s. The reflected power of the ICP generator was 15 W, and the direct-current bias was ∼200 V. After etching, the coupons were immersed in an acetone solution in an ultrasonic bath to remove photoresist residues. After that, EG growth was performed as described in the previous section.[32,35−37]

2.3. Characterization. A Zeiss Supra 55VP scanning electron microscope was employed for surface imaging. Raman spectra were collected with a WiTec Raman microscope using a green laser (532 nm); the Raman spectra shown in this work are the average of 2500 single spectra collected over a 100 μm^2 area map. An electrochemical workstation (CH Instruments, 660 E model) was used to assess the electrochemical performance of the cells operating in a three-probe configuration. The primary electrochemical properties of the 3C-SiC films and the EG grown on SiC films were characterized in a three-electrode cell using a solution of 0.1 M phosphate-buffered saline (PBS) as an electrolyte, with respect to Ag/AgCl electrodes. Electrochemical impedance spectroscopy (EIS) measurements were conducted in the 0.01 Hz to 1 kHz frequency range with a signal amplitude of 5 mV.

2.4. On-Skin Measurements and Headband Tests. The on-skin EIS tests were performed by mounting the EG sensors on the forehead and back of the head. Double-sided carbon tape was attached to the back of the highly doped silicon substrate using a pin button for electrical connection.

In all on-skin measurements, a two-electrode setup was configured using the EG sensor as the working electrode and the Ag/AgCl gel electrode as the reference electrode. All of the EIS measurements were taken across a frequency range of 0.1 to 1000 Hz at 5 mV. Eight EG sensors were tested for each fabricated pattern, and the sensors were tested 10 times to investigate reproducibility. Each sensor was first tested in a three-electrode cell setup.

Subsequently, on-skin EIS measurements were performed on the forehead and occipital region with 5 mm hair size of the head by accommodating graphene sensors in an elastic headband. Five forehead EIS sequential measurements were taken at 5-min intervals without breaking contact with the skin. Each complete measurement took 3−4 min. The average impedance values and their variation were evaluated in the stable value region, reached after 3−5 repeated measurements.[32]

Finally, the elastic headband setup was modified to accommodate eight sensor channels for measurements on the occipital region. The same setup was used to test sequentially eight hexagonal-patterned epitaxial graphene (HPEG), eight flat epitaxial graphene (FEG), and eight wet sensors for a direct performance comparison.

2.5. S/N Ratio Calculation. The S/N ratio is the ratio of a signal's power spectral density (PSD) to the power of the background noise.[38,39] The S/N ratio from the EEG recording is calculated from eq 1[39] as follows:

$$\mathrm{S/N} = 10 \log \frac{\frac{1}{N}\sum_{i=1}^{N}(\mathrm{PSDup})}{\frac{1}{N'}\sum_{j=1}^{N'}(\mathrm{PSDdown})}\ (\mathrm{dB}) \quad (1)$$

Here, N is the signal considered as the number of up states, N' is the noise considered as the number of down states, PSDup is the power spectral density of the signal, and PSDdown is the power spectral density of the noise.[39]

2.6. Communication with Robotic Systems. The user used our augmented brain−robot interface (aBRI) platform to control the robot systems. The aBRI platform allows the user to interact with machines/robots in more natural forms, which is better than the conventional brain−computer interface (BCI) application setting, which requires users to remain stationary. The aBRI platform consists of four main components: (i) devices for interfaces, (ii) a mobile EEG system, (iii) a single board computer, and (iv) a robot system. All of these main components are communicated via the transmission control protocol/internet protocol (TCP/IP). (i) The device for the interface of this study was a mobile phone (Samsung A31, 64GB 4GB RAM, 6.4 in. display size, 1080 × 2400 pixels display resolution) and augmented reality headset (Hololens 2, Microsoft, USA). (ii) The wireless mobile EEG system was Mentalab Explore system with eight channels (Mentalab US LLC/2670 Worden St #19, San Diego, CA). (iii) The single board computer was a Rasberry PI 4B (RPi4) used as the central hub to exchange the event communication among devices/systems. (iv) The robot system was Quadrupedal Unmanned Ground Vehicles, or Q-UGVs (Ghost Robotics Corp., Philadelphia, PA). In this study, the individual/user was first trained with the mobile phone interfaces to familiarize themselves with the aBRI platform and BCI applications, and then they interacted with the Q-UGVs robot via HoloLens with our developed sensors integrated into the mobile EEG system.

https://doi.org/10.1021/acsanm.2c05546
ACS Appl. Nano Mater. 2023, 6, 5440−5447

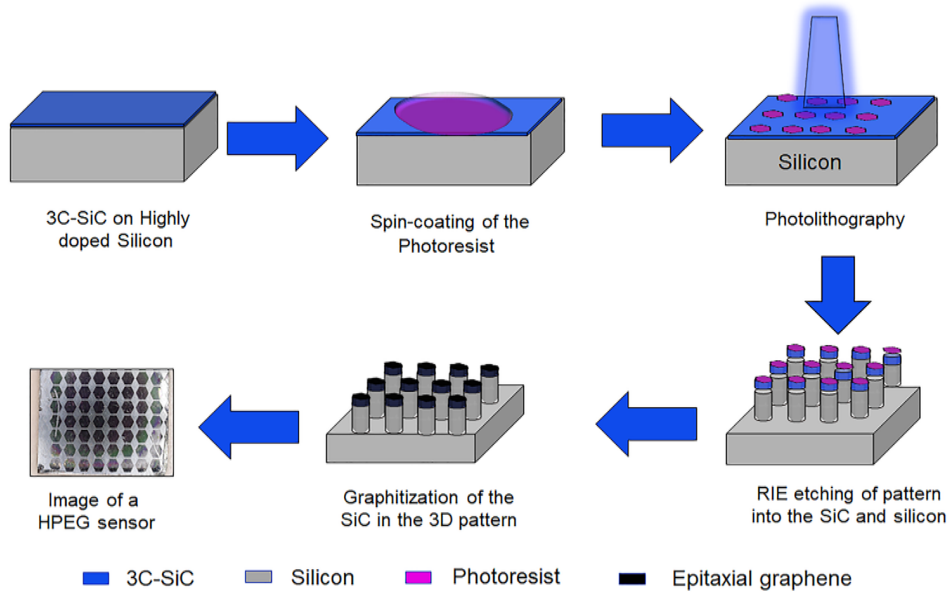

Figure 1. Schematic of the fabrication process of the micropatterned graphene sensor.

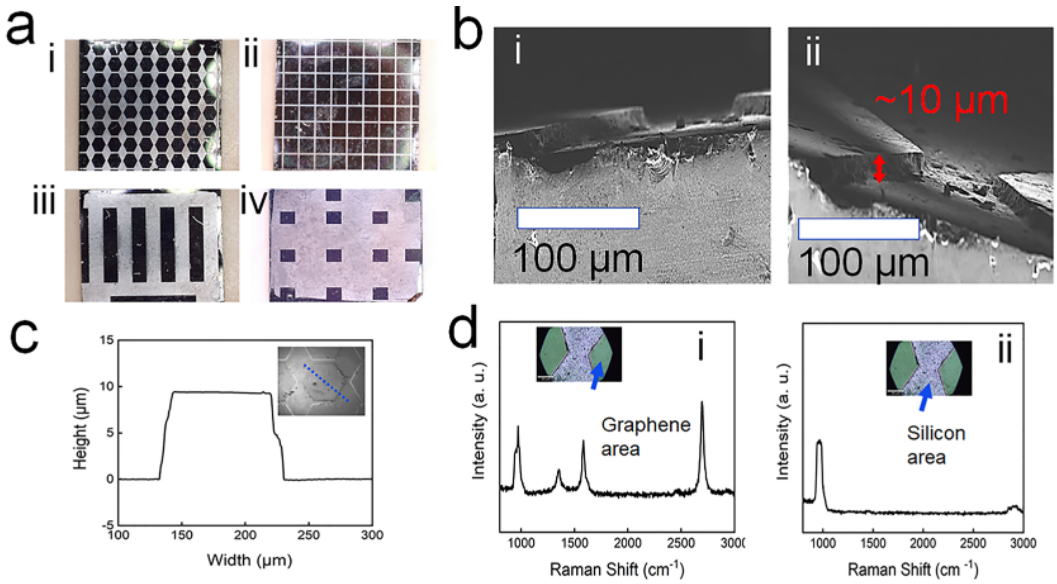

Figure 2. (a) Microscope images of four sensor patterns (squares, hexagons, bars, and dots). (b) SEM cross-sectional images of the micropatterns. (c) Micropattern height measured with a profilometer along the dotted line in the inset. (d) Raman spectroscopy of micropatterned graphene sensors: (i) patterned graphene area; (ii) silicon area.

3. RESULTS AND DISCUSSION

We fabricated three-dimensional structures (~10 μm in height) by etching SiC and the silicon substrate according to a series of different patterns and shapes in the small (1−5 mm^2) size range with varying densities. The schematic of the fabrication process of the three-dimensional micropatterned EG sensors is shown in Figure 1. Films of 3C-SiCof 500 nm thickness, heteroepitaxially grown on highly doped silicon substrates, were used as the starting materials. Photolithography was then performed, followed by RIE. The total etching duration was timed to etch the entire SiC film plus several microns into the silicon substrate. After the SiC/silicon patterning, a catalytic alloy method[34,35] was employed for the growth of EG around the surfaces of the SiC on the tip of the formed structures (Figure 1).

In this work, we chose four sensor patterns: square-patterned epitaxial graphene (SPEG), HPEG, pillar-patterned epitaxial graphene (PPEG), and dot-patterned epitaxial graphene (DPEG). Unpatterned EG sensors,[32] FEG, were used as a reference. The microscope images of the four types of patterned sensors are shown in Figure 2a, while the total area of the electrode structures is reported in Table 1. Scanning electron microscopy (SEM) was employed to measure the depth of the etching through the cross section of the patterns (Figure 2b). The SEM confirmed that the structures' depth is around 10 μm from the top surface. The depth was also confirmed using a contact profilometer (Figure 2c), matching well with the information from the cross-sectional measurement via SEM.

https://doi.org/10.1021/acsanm.2c05546
ACS Appl. Nano Mater. 2023, 6, 5440−5447

Table 1. Comparison of Graphene Coverage and Averaged Impedance Values for EG Sensors, Unpatterned (FEG) and Patterned with the Four Chosen Designs: Square (SPEG), Hexagonal (HPEG), Pillar (PPEG), and Dot (DPEG)[a]

graphene sensor	total surface area of graphene (cm^2)	impedance in a PBS solution at 50 Hz (Ω)	on-skin impedance (forehead) at 50 Hz (kΩ)	on-skin impedance (occipital) at 50 Hz (kΩ)
FEG	1.0	130 ± 10	75 ± 10	295 ± 10
SPEG	0.81	138 ± 10	95 ± 10	260 ± 10
HPEG	0.72	150 ± 10	110 ± 10	155 ± 10
PPEG	0.48	168 ± 10	125 ± 10	195 ± 10
DPEG	0.2	180 ± 10	130 ± 10	325 ± 10

[a]For more specific dimensions, see the Supporting Information.

Raman spectroscopy mapping was conducted on etched and nonetched areas of the samples. The averaged Raman spectra of nonetched regions (top of the structures) show, in addition to silicon peaks, four dominant peaks: the LO peak of SiC at ∼970 cm^{-1} and graphene-related peaks of the D peak at ∼1340 cm^{-1}, G peak at ∼1580 cm^{-1}, and 2D peak at ∼2680 cm^{-1} [Figure 2d(i)],[40,41] whereas the Raman spectra from the areas at the bottom/valleys of the pattern only show the silicon response with no presence of SiC or graphene [Figure 2d(ii)]. The inset shows the microscope images of the graphene area (greenish) [Figure 2d(i)] and the etched silicon area (gray) [Figure 2d(ii)]. The intensity ratios between the D and G bands and those of the 2D and G peaks can be used to estimate the average domain sizes and the number of graphene layers, respectively.[35,42,43] The I_D/I_G (0.238) and I_{2D}/I_G (3.2) average intensity ratios of the micropatterned graphene indicate here the presence of 1−2 layers with an average graphene domain size below 100 nm, consistent with the approach used for EG growth.[32,35] This also indicates the subnanometer thickness of the layer in contact with the skin.

The EIS technique was employed to quantify and compare the electrochemical properties of the micropatterned EG sensors in 0.1 M PBS solution in a three-electrode system. From the EIS measurements, the EG sensors show low resistive behavior in the range of 130 ± 10 to 180 ± 10 Ω at a frequency of 50 Hz (Figure 3a and Table 1). In particular, it is observed from both the Nyquist and Bode plots in Figure 3a,b that the FEG and SPEG sensors show the lowest impedance in the PBS solution.

On-skin (forehead) measurements were then performed using four sensor channels as working electrodes (Figure 4a). An Ag/AgCl sensor attached to the mastoid position was used as the reference electrode. The on-skin Nyquist plots show typical hemisphere behavior because human skin is more resistive (in the kiloohm range) compared to the PBS solution (Figure 3c). The Bode plot in Figure 3d indicates on-skin impedance for the EG sensors on the forehead ranging from 75 ± 10 to 130 ± 10 kΩ at 50 Hz. Once again, FEG sensors show the lowest impedance and DPEG sensors the highest impedance, a trend appearing to be directly correlated with their total graphene surface area (Table 1).

Subsequently, we have investigated the performance of the sensors when placed on the occipital region of the head. Visual BCI paradigms, like the SSVEP, are based on monitoring of the visual cortex activity in correspondence to this region of the head.[5]

The impedance values of the different micropatterned EG sensors measured on the occipital area of an individual with short hair (5 mm in length) are reported in Table 1. From the table, it is found that, even though the FEG and SPEG sensors showed low impedance in the PBS solution and on the fairly flat and nonhairy skin of the forehead, thanks to their largest graphene surface coverage, they yielded the highest contact impedances in the occipital area of the scalp. Instead, the HPEG design yielded the lowest on-skin impedance in this critical test. We believe that in this test the total graphene area available for contacting the skin no longer correlates with the actual amount of area able to achieve useful contact because of the curved and hairy nature of the occipital surface of the scalp.

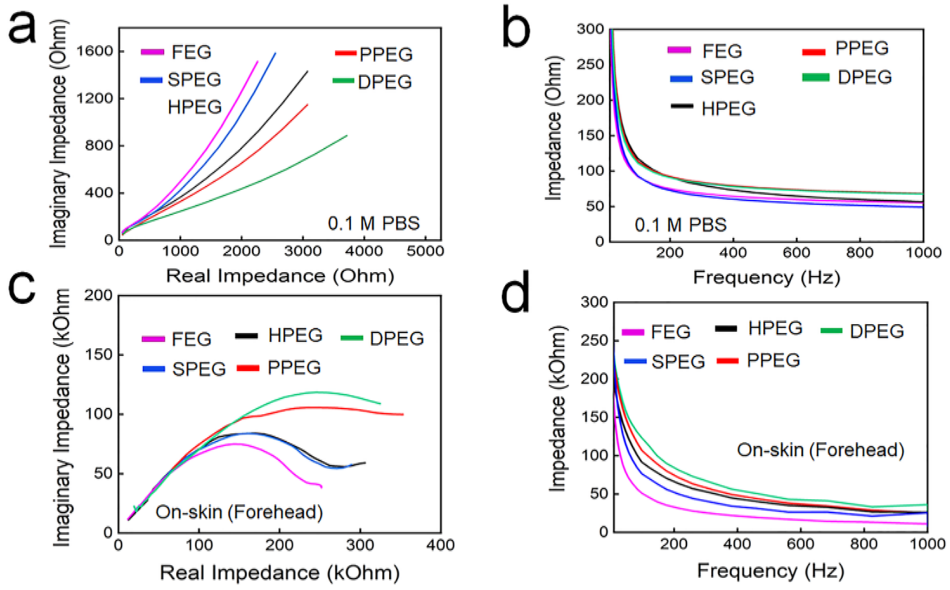

Figure 3. Comparison of (a) Nyquist and (b) Bode plots of the four micropatterned sensor types plus the unpatterned FEG in a three-electrode system, using a 0.1 M PBS solution as the electrolyte. (c) Nyquist and (d) Bode plots of the same sensors when placed in contact with the forehead (nonhairy skin).

https://doi.org/10.1021/acsanm.2c05546
ACS Appl. Nano Mater. 2023, 6, 5440−5447

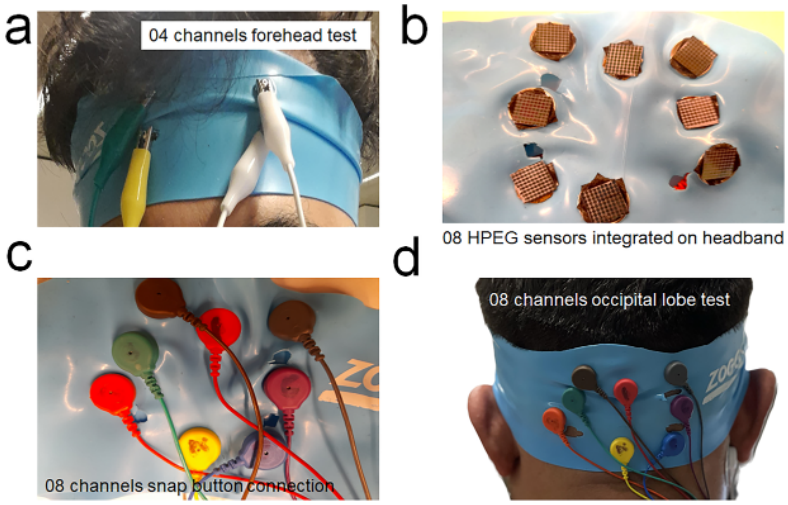

Figure 4. (a) Image of the impedance measurement setup using four-channel graphene sensors on the forehead. (b) Arrangement of the eight-channel HPEG sensors on an elastic headband. (c) Image of the snap button connection on the back of the sensors. (d) Headband with eight-channel EG sensors on the occipital region of the scalp with of 5.0 mm hair.

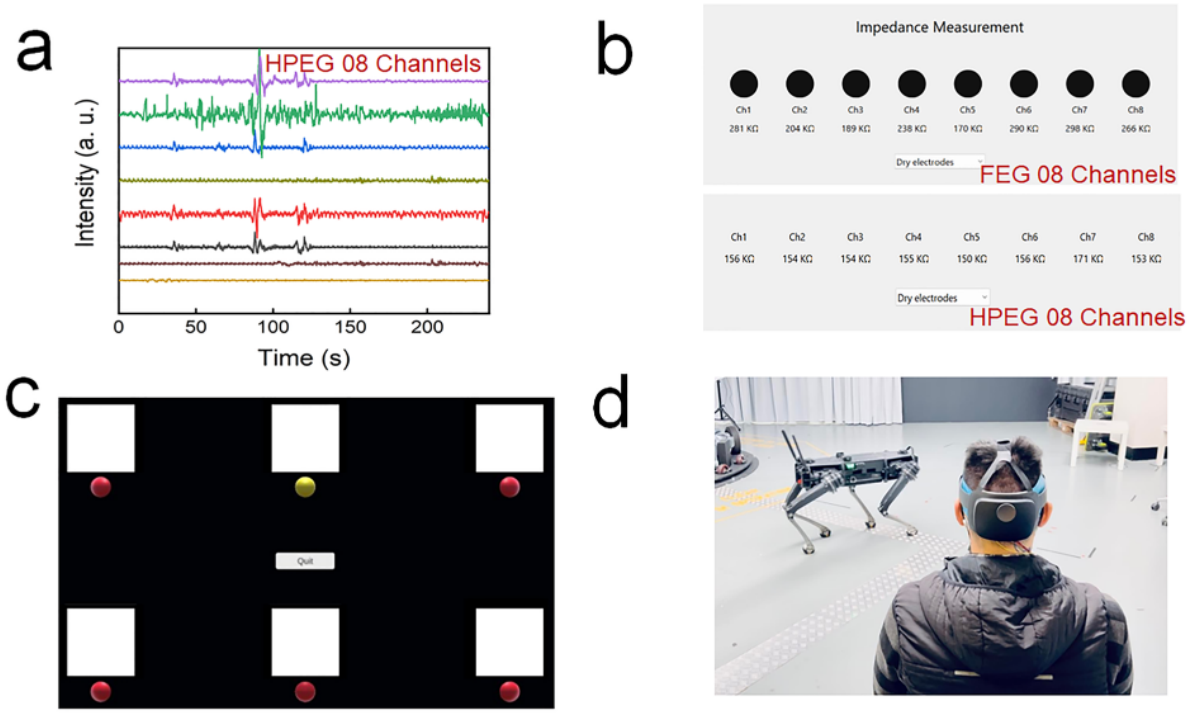

Figure 5. (a) EEG signal recorded by eight-channel HPEG sensors from the occipital region. (b) Impedance values of eight-channel FEG and eight-channel HPEG sensor systems placed on the occipital area of the head. (c) Image of the flickering visual labels showing eight possible command choices to the individual. (d) Commanding a quadruped robot using the BMI system based on the HPEG sensors.

It appears that the hexagonal shape and packing factor in the design of the HPEG structures (see the Supporting Information) is able to strike a better balance between the total available graphene area for contact and the effectively achieved contact area with the occipital scalp, likely also more accommodating for the presence of short hair.

Based on this observation, an eight-channel HPEG sensor system was prepared using an elastic headband (Figure 4b,c). The sensors were placed as an irregular array in correspondence to the occipital region (Figure 4d). The EEG signals were recorded using the Mentalab Explore mobile EEG device. All eight channels detected EEG signals (Figure 5a), although a large variation in the S/N ratio of each channel was observed, correlated not with the sensor quality but with its specific location and the specific pressure applied on the scalp. These parameters appear, hence, crucial for signal acquisition. The elastic band pressure is not necessarily transferred uniformly on all areas of the head because it also depends on the local curvature and hair distribution.[14,20] For comparisons, an equivalent eight-channel unpatterned sensor system was also tested, and it was confirmed that the HPEG sensors show

https://doi.org/10.1021/acsanm.2c05546
ACS Appl. Nano Mater. 2023, 6, 5440−5447

better performance than the FEG sensors on the occipital region.

The eight-channel system embedded in the elastic headband was then subsequently connected with the mobile EEG amplifier in the aBRI platform to test the BMI operation. Stimulation was performed using visual labels flickering at different frequencies on either a mobile phone screen (training) (Figure 5c) or an augmented reality headset, HoloLens 2 (testing). The HPEG sensors were used to measure the activity elicited at the visual cortex by the flicker stimulus. Then the acquired brain signal was used as input for the classifier in the single-board computer to detect the corresponding flicker that the user was visually focusing on.[11] Finally, the single-board computer sent the classifier's output to issue the command to the robot system (here, a Q-UGVs robot from Ghost Robotics; Figure 5d). The HPEG-based interface system achieved 94% accuracy on average from six commands (see Figure S1 for additional details).

Finally, we compared the S/N ratios of the eight HPEG sensor channels contacting the occipital area with those of a system using eight silver-based wet sensors (Figure 6a,b and Table 2).

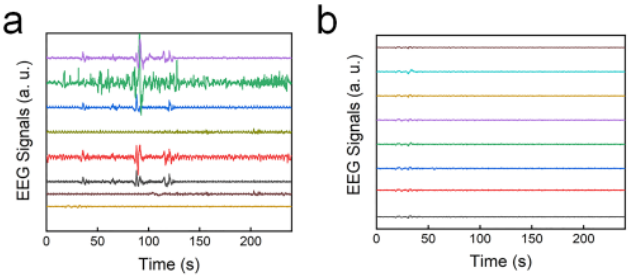

Figure 6. (a) EEG signal acquisition with the eight-channel HPEG sensors. (b) EEG signal acquisition with the eight-channel wet sensor system.

Table 2. Comparison of S/N Values of Each Channel for HPEG and Ag/AgCl Wet Sensors

	S/N (dB)	
channel	HPEG sensor	Ag/AgCl sensor
1	15 ± 5	30 ± 5
2	5 ± 5	30 ± 5
3	15 ± 5	30 ± 5
4	15 ± 5	30 ± 5
5	10 ± 5	30 ± 5
6	18 ± 5	30 ± 5
7	15 ± 5	30 ± 5
8	25 ± 5	30 ± 5

As expected, as the gold standard, the wet sensors showed a high S/N ratio of 30 dB compared to the HPEG sensors. As previously remarked, the HPEG system channels also show strong variability due to circumstances that are hard to control in the present prototype. However, channel 8 indicates a S/N of 25 dB, which is fairly close to that of the wet sensors. This result provides the promise that, with a specifically tailored helmet and improved sensor placement and applied pressure, EG sensors are able to achieve a satisfactory S/N performance close to that of the wet sensors.

4. CONCLUSIONS

We have fabricated micropatterned, compact EG EEG sensors on SiC on silicon, where the graphene layer in contact with the skin is on average thinner than a nanometer. We have fabricated structures of about 10 μm deep using designs with different shapes and packing factors to enable their use on the occipital area of the head. Overall, we have observed that while the contact impedance of the sensors with the flat skin of the forehead correlates with the total amount of graphene area available, when the sensors are applied on the occipital area, this correlation no longer holds. While this study was not meant to deliver a final design, we do observe that an ideal design needs to strike a balance between the total available graphene area and other factors, including the capability to accommodate for the presence of hair and the capability to transfer adequate contact pressure.

We have successfully employed the hexagonal structure design (HPEG) to acquired the EEG signal from the occipital area of an individual with 5-mm-long hair. These sensors yielded a low average impedance of 155 ± 10 kΩ at 50 Hz and a satisfactory S/N ratio with the capability of reaching up to 25 ± 5 dB, which is a value very close to the gold standard.

Finally, we also demonstrated a full BMI system to control a quadruped robot via the SSVEP paradigm using an eight-channel HPEG sensor array with 94% accuracy.

We point out that monitoring EEG from the occipital region of the head with dry sensors is a particularly challenging endeavor and that, for a given design, the observed variability originates from the exact placement of the sensor rather than the individual sensor's properties. Wet sensors are not prone to such variability. Even though, at present, matching the signal acquisition performance of wet Ag/AgCl sensors with that of dry sensors is still challenging in practical applications, we believe these three-dimensional micropatterned EG sensors represent one solid step forward toward this goal.

■ ASSOCIATED CONTENT

Supporting Information

The Supporting Information is available free of charge at https://pubs.acs.org/doi/10.1021/acsanm.2c05546.

Analysis of the geometrical nanopatterns and evaluation of the BCI accuracy (PDF)

■ AUTHOR INFORMATION

Corresponding Author

Francesca Iacopi − *School of Electrical and Data Engineering, Faculty of Engineering and Information Technology, and Australian Research Council Centre of Excellence for Transformative Meta-Optical Systems, University of Technology Sydney, Ultimo, NSW 2007, Australia;* orcid.org/0000-0002-3196-0990; Email: francesca.iacopi@uts.edu.au

Authors

Shaikh Nayeem Faisal − *School of Electrical and Data Engineering, Faculty of Engineering and Information Technology, University of Technology Sydney, Ultimo, NSW 2007, Australia;* orcid.org/0000-0003-3317-2282

Tien-Thong Nguyen Do − *Australian Artificial Intelligence Institute, FEIT, University of Technology Sydney, Ultimo, NSW 2007, Australia;* orcid.org/0000-0002-8597-5944

https://doi.org/10.1021/acsanm.2c05546
ACS Appl. Nano Mater. 2023, 6, 5440−5447

Tasauf Torzo − *School of Electrical and Data Engineering, Faculty of Engineering and Information Technology, University of Technology Sydney, Ultimo, NSW 2007, Australia*

Daniel Leong − *Australian Artificial Intelligence Institute, FEIT, University of Technology Sydney, Ultimo, NSW 2007, Australia;* orcid.org/0000-0002-1678-5629

Aiswarya Pradeepkumar − *School of Electrical and Data Engineering, Faculty of Engineering and Information Technology, University of Technology Sydney, Ultimo, NSW 2007, Australia;* orcid.org/0000-0003-0669-5459

Chin-Teng Lin − *Australian Artificial Intelligence Institute, FEIT, University of Technology Sydney, Ultimo, NSW 2007, Australia;* orcid.org/0000-0001-8371-8197

Complete contact information is available at: https://pubs.acs.org/10.1021/acsanm.2c05546

Notes

The authors declare no competing financial interest.

■ ACKNOWLEDGMENTS

C.-T.L. and F.I. acknowledge funding from the Defence Innovation Hub, an initiative of the Australian Government (Contract P18-650825). David Katzmarek from the University of Technology Sydney is acknowledged for support with photolithography. The authors also acknowledge support by the Australian National Fabrication Facility, part of the University of Technology Sydney, and support by the Research & Prototype Foundry at the University of Sydney Nano Institute.

■ REFERENCES

(1) Zhang, M.; Tang, Z.; Liu, X.; Van der Spiegel, J. Electronic neural interfaces. *Nat. Electron.* **2020**, *3*, 191−200.

(2) Donoghue, J. P. Connecting cortex to machines: recent advances in brain interfaces. *Nat. Neurosci.* **2002**, *5*, 1085−1088.

(3) Hochberg, L. R.; Bacher, D.; Jarosiewicz, B.; Masse, N. Y.; Simeral, J. D.; Vogel, J.; Haddadin, S.; Liu, J.; Cash, S. S.; van der Smagt, P.; Donoghue, J. P. Reach and grasp by people with tetraplegia using a neurally controlled robotic arm. *Nature* **2012**, *485*, 372−375.

(4) Rich, S. I.; Wood, R. J.; Majidi, C. Untethered soft robotics. *Nat. Electron.* **2018**, *1*, 102−112.

(5) Iacopi, F.; Lin, C.-T. A perspective on electroencephalography sensors for brain-computer interfaces. *Prog. Biomed. Eng.* **2022**, *4*, 043002.

(6) Parvizi, J.; Kastner, S. Promises and limitations of human intracranial electroencephalography. *Nat. Neurosci.* **2018**, *21*, 474−483.

(7) Sung, C.; Jeon, W.; Nam, K. S.; Kim, Y.; Butt, H.; Park, S. Multimaterial and multifunctional neural interfaces: from surface-type and implantable electrodes to fiber-based devices. *J. Mater. Chem. B* **2020**, *8*, 6624−6666.

(8) Yang, L.; Liu, Q.; Zhang, Z.; Gan, L.; Zhang, Y.; Wu, J. Materials for dry electrodes for the electroencephalography: Advances, Challenges, Perspectives. *Adv. Mater. Technol.* **2022**, *7* (3), 2100612.

(9) Veena, N.; Anitha, N. A review of non-invasive BCI devices. *Int. J. Biomed. Eng. Technol.* **2020**, *34*, 205−233.

(10) McFarland, D. J.; Wolpaw, J. R. EEG-based brain−computer interfaces. *Curr. Opin. Biomed. Eng.* **2017**, *4*, 194−200.

(11) Lin, C.-T.; Do, T. -T. N. Direct-sense brain−computer interfaces and wearable computers. *IEEE Trans. Syst. Man Cybern. Syst.* **2021**, *51*, 298−312.

(12) Habibzadeh Tonekabony Shad, E.; Molinas, M.; Ytterdal, T. Impedance and noise of passive and active dry EEG electrodes: A Review. *IEEE Sens. J.* **2020**, *20*, 14565−14577.

(13) Yang, L.; Gan, L.; Zhang, Z.; Zhang, Z.; Yang, H.; Zhang, Y.; Wu, J. Insight into the contact impedance between the electrode and the skin surface for electrophysical recordings. *ACS Omega* **2022**, *7* (16), 13906−13912.

(14) Hajare, R.; Kadam, S. Comparative study analysis of practical EEG sensors in medical diagnoses. *Global Transition Proceedings* **2021**, *2*, 467−475.

(15) Liao, L.-D.; Wang, I.-J.; Chen, S.-F.; Chang, J.-Y.; Lin, C. T. Design, fabrication and experimental validation of a novel dry-contact sensor for measuring electroencephalography signals without skin preparation. *Sensors* **2011**, *11* (6), 5819−5834.

(16) Liao, L.-D.; Chen, C.-Y.; Wang, I.-J.; Chen, S.-F.; Li, S.-Y.; Chen, B.-W.; Chang, J.-Y.; Lin, C.-T. Gaming control using a wearable and wireless EEG-based brain-computer interface device with novel dry foam-based sensors. *J. Neuroeng. Rehab.* **2012**, *9*, 5.

(17) Lopez-Gordo, M. A.; Sanchez-Morillo, D.; Valle, F. P. Dry EEG electrodes. *Sensors* **2014**, *14* (7), 12847−12870.

(18) Heijs, J. J. A.; Havelaar, R. J.; Fiedler, P.; van Wezel, R. J. A.; Heida, T. Validation of soft multipin dry EEG electrodes. *Sensors* **2021**, *21*, 6827.

(19) Kostarelos, K.; Vincent, M.; Hebert, C.; Garrido, J. A. Graphene in the design and engineering of next-generation neural interfaces. *Adv. Mater.* **2017**, *29*, 1700909.

(20) Faisal, S. N.; Iacopi, F. Thin-film electrodes based on two-dimensional nanomaterials for neural interfaces. *ACS Appl. Nano Mater.* **2022**, *5* (8), 10137−10150.

(21) Singh, E.; Meyyappan, M.; Nalwa, H. S. Flexible graphene-based wearable gas and chemical sensors. *ACS Appl. Mater. Interfaces* **2017**, *9* (40), 34544−34586.

(22) Krishnan, S. K.; Singh, E.; Singh, P.; Meyyappan, M.; Nalwa, H. S. A review on graphene-based nanocomposites for electrochemical and fluorescent biosensors. *RSC Adv.* **2019**, *9*, 8778−8881.

(23) Wu, N.; Wan, S.; Su, S.; Huang, H.; Dou, G.; Sun, L. Electrode materials for brain-machine interface: A review. *InfoMat* **2021**, *3* (11), 1174−1194.

(24) Wang, X.; Sun, X.; Gan, D.; Soubrier, M.; Chiang, H.-S.; Yan, L.; Li, Y.; Li, J.; Yu, S.; Xia, Y.; Wang, K.; Qin, Q.; Jiang, X.; Han, L.; Pan, T.; Xie, C.; Lu, X. Bioadhesive and conductive hydrogel integrated bran-machine interfaces for conformal and immune-evasive contact with brain tissue. *Matter* **2022**, *5* (4), 1204−1223.

(25) Won, C.; Jeong, U.-J.; Lee, S.; Lee, M.; Kwon, C.; Cho, S.; Yoon, K.; Lee, S.; Chun, D.; Cho, I.-J.; Lee, T. Mechanically tissue-like and highly conductive Au nanoparticles embedded elastomeric fiber electrodes of brain-machine interfaces for chronic in vivo brain neural recording. *Adv. Funct. Mater.* **2022**, *32* (52), 2205145.

(26) Sun, B.; McCay, R. N.; Goswami, S.; Xu, Y.; Zhang, C.; Ling, Y.; Lin, J.; Yan, Z. Gas-permeable, multifunctional on-skin electronics based on laser-induced porous graphene and sugar-templated elastomer sponges. *Adv. Mater.* **2018**, *30*, 1804327.

(27) Qiu, J.; Yu, T.; Zhang, W.; Zhao, Z.; Zhang, Y.; Ye, G.; Zhao, Y.; Du, X.; Liu, X.; Yang, L.; Zhang, L.; Qi, S.; Tan, Q.; Guo, X.; Li, G.; Guo, S.; Sun, H.; Wei, D.; Liu, N. A bioinspired, durable, and nondisposable transparent graphene skin electrode for electrophysiological signal detection. *ACS Mater. Lett.* **2020**, *2*, 999−1007.

(28) Ameri, S. K.; Kim, M.; Kuang, I. A.; Perera, W. K.; Alshiekh, M.; Jeong, H.; Topcu, U.; Akinwande, D.; Lu, N. Imperceptible electrooculography graphene sensor system for human−robot interface. *NPJ. 2D Mater. Appl.* **2018**, *2*, 19.

(29) Li, Z.; Guo, W.; Huang, Y.; Zhu, K.; Yi, H.; Wu, H. On-skin graphene electrodes for large area electrophysiological monitoring and human-machine interfaces. *Carbon* **2020**, *164*, 164−170.

(30) Driscoll, N.; Erickson, B.; Murphy, B. B.; Richardson, A. G.; Robbins, G.; Apollo, N. V.; Mentzelopoulos, G.; Mathis, T.; Hantanasirisakul, K.; Bagga, P.; Gullbrand, S. E.; Sergison, M.; Reddy, R.; Wolf, J. A.; Chen, H. I.; Lucas, T. H.; Dillingham, T. R.; Davis, K. A.; Gogotsi, Y.; Medaglia, J. D.; Vitale, F. MXene-infused bioelectronic interfaces for multiscale electrophysiology and stimulation. *Sci. Trans. Med.* **2021**, *13*, 612.

(31) Loussouarn, G.; Lozano, I.; Panhard, S.; Collaudin, C.; El Rawadi, C.; Genain, G. Diversity in human hair growth, diameter, colour and shape. An in vivo study on young adults from 24 different ethnic groups observed in the five continents. *Euro. J. Dermatology* **2016**, *26*, 144−154.
(32) Faisal, S. N.; Amjadipour, M.; Izzo, K.; Singer, J. A.; Bendavid, A.; Lin, C.-T.; Iacopi, F. Non-invasive on-skin sensors for brain machine interfaces with epitaxial graphene. *J. Neural Eng.* **2021**, *18*, 066035.
(33) Abiri, R.; Borhani, S.; Sellers, E. W.; Jiang, Y.; Zhao, X. A comprehensive review of EEG-based brain-computer interface paradigms. *J. Neural Eng.* **2019**, *16*, 011001.
(34) Portail, M.; Zielinski, M.; Chassagne, T.; Roy, S.; Nemoz, M. Comparative study of the role of the nucleation stage on the final crystalline quality of (111) and (100) silicon carbide films deposited on silicon substrates. *J. Appl. Phys.* **2009**, *105* (8), 083505.
(35) Mishra, N.; Boeckl, J. J.; Tadich, A.; Jones, R. T.; Pigram, P. J.; Edmonds, M.; Fuhrer, M. S.; Nichols, B. M.; Iacopi, F. Solid source growth of graphene with Ni−Cu catalysts: towards high quality in situ graphene on silicon. *J. Phys. D Appl. Phys.* **2017**, *50* (9), 095302.
(36) Iacopi, F.; Mishra, N.; Cunning, B. V.; Goding, D.; Dimitrijev, S.; Brock, R.; Dauskardt, R. H.; Wood, B.; Boeckl, J. A catalytic alloy approach for graphene on epitaxial SiC on silicon wafers. *J. Mater. Res.* **2015**, *30* (5), 609−616.
(37) Pradeepkumar, A.; Amjadipour, M.; Mishra, N.; Liu, C.; Fuhrer, M. S.; Bendavid, A.; Isa, F.; Zielinski, M.; Sirikumara, H. I.; Jayasekara, T.; Gaskill, D. K.; Iacopi, F. p-Type epitaxial graphene on cubic silicon carbide on silicon for integrated silicon technologies. *ACS Appl. Nano Mater.* **2020**, *3*, 830−841.
(38) Sanchez-Vives, M. V.; McCormick, D. A. Cellular and network mechanisms of rhythmic recurrent activity in neocortex. *Nat. Neurosci.* **2000**, *3*, 1027−1034.
(39) Suarez-Perez, A.; Gabriel, G.; Rebollo, B.; Illa, X.; Guimerà-Brunet, A.; Hernández-Ferrer, J.; Martinez, M. T.; Villa, R.; Sanchez-Vives, M. V. Quantification of signal-to-noise ratio in cerebral cortex recordings using flexible MEAs with co-localized platinum black, carbon nanotubes, and gold electrodes. *Front. Neurosci.* **2018**, *12*, 862.
(40) Cunning, B. V.; Ahmed, M.; Mishra, N.; Kermany, A. R.; Wood, B.; Iacopi, F. Graphitized silicon carbide microbeams: wafer-level, self-aligned graphene on silicon wafers. *Nanotechnology* **2014**, *25* (32), 325301.
(41) Mishra, N.; Boeckl, J.; Motta, N.; Iacopi, F. Graphene growth on silicon carbide: A review. *Physica Status Solidi (a)* **2016**, *213* (9), 2277.
(42) Malard, L.; Pimenta, M.; Dresselhaus, G.; Dresselhaus, M. Raman spectroscopy in graphene. *Phys. Rep.* **2009**, *473* (5), 51−87.
(43) Ferrari, A. C. Raman spectroscopy of graphene and graphite: disorder, electron−phonon coupling, doping and nonadiabatic effects. *Solid State Commun.* **2007**, *143* (1), 47−57.

https://doi.org/10.1021/acsanm.2c05546
ACS Appl. Nano Mater. 2023, 6, 5440−5447